



CHALMERS
UNIVERSITY OF TECHNOLOGY

Free-standing 3D-printed monoliths of SrCl_2 for ammonia storage as a hydrogen carrier

Downloaded from: <https://research.chalmers.se>, 2025-05-31 23:35 UTC

Citation for the original published paper (version of record):

Shezad, N., D'Agostini, M., Ezzine, A. et al (2025). Free-standing 3D-printed monoliths of SrCl_2 for ammonia storage as a hydrogen carrier. *International Journal of Hydrogen Energy*, 134: 1-9. <http://dx.doi.org/10.1016/j.ijhydene.2025.04.432>

N.B. When citing this work, cite the original published paper.



Free-standing 3D-printed monoliths of SrCl₂ for ammonia storage as a hydrogen carrier

Nasir Shezad^a, Marco D'Agostini^b, Ali Ezzine^b, Giorgia Franchin^b, Paolo Colombo^b, Zhejian Cao^{c,*}, Farid Akhtar^{a,**}

^a Division of Materials Science, Department of Engineering Sciences and Mathematics, Luleå University of Technology, Luleå, SE-971 87, Sweden

^b Department of Industrial Engineering, University of Padova, Via Marzolo, 9, Padova, 35131, Italy

^c Systems and Synthetic Biology Division, Department of Life Sciences, Chalmers University of Technology, SE-412 96, Gothenburg, Sweden

ARTICLE INFO

Keywords:

Hydrogen
Ammonia
Sorption
Kinetics
Metal halides
3D-printing

ABSTRACT

The alkaline earth metal halides (AEMHs), such as strontium chloride (SrCl₂), are promising sorbents for hydrogen storage in the form of ammonia. However, these sorbents suffer from structural disintegration problems due to the extraordinary volume expansion during ammonia sorption. This study reports the fabrication of 3D-printed SrCl₂ monoliths scaffolded with bentonite using the direct ink writing technique. The optimized monolith with a 60 % SrCl₂ loading exhibited an ammonia storage capacity of 488 mg/g, maintaining remarkable structural integrity and effectively accommodating volumetric changes during sorption and desorption over 20 cycles. The kinetics data revealed that ammonia sorption followed a pseudo-second-order model, and intercrystalline diffusion was the rate-controlling step in the 3D-printed SrCl₂ structures. High-pressure sorption isotherms were explained by the dual-site Langmuir-Freundlich model due to surface heterogeneity in terms of energies and binding sites for metal-amine complex formation. Thus, cognitively designed AEMHs monoliths present the potential for ammonia storage in various applications by effectively overcoming structural challenges.

1. Introduction

Energy dynamics are undergoing rapid transformations, and global leaders are committed to achieving the zero-carbon emission target [1]. A carbon-free energy model can be established by generating the cleanest hydrogen [2,3]. Besides the production of hydrogen, challenges associated with hydrogen storage and transportation need to be addressed [4,5]. Different methodologies for hydrogen storage can be used, including physical storage [6], carrier materials (hydrogen-rich chemicals) [7], or solid matrix systems [8]. Physical storage of hydrogen as a liquid at cryogenic temperatures (−252 °C) or compressing it up to 70 MPa demands substantial energy input to maintain the necessary pressure and temperature conditions. Alternatively, hydrogen-rich chemicals such as ammonia (NH₃), methanol, ethanol, and formic acid methanol can be considered [6,9]. Among hydrogen-rich chemicals, NH₃ is the only carbon-free chemical. Therefore, storing hydrogen in the form of NH₃ could be a promising strategy, which could allow for its direct use as a fuel and source of hydrogen [10]. Usually, NH₃ is stored in

a liquid state, which faces several criticalities, including the risk of leakage, and requires special containers with a cooling system as well as high-pressure provision, leading to an energy-intensive system [11,12]. Alternatively, solid sorbents could be a substitute, offering the advantage of higher NH₃ packing density at room temperature. The sorbents can release NH₃ by lowering pressure and heating at a mild temperature [13,14]. Additionally, NH₃ storage using solid sorbents exhibits lower vapor pressure and a reduced risk of toxicity, flammability, and explosion. These merits render the sorption technique an alternative potential H₂ storage option in the form of NH₃ [13].

Several solid sorbents have been explored for NH₃ storage, such as zeolites [15], activated carbon [16], metal-organic frameworks [17], and metal hydride and halides [8,18]. Among these sorbents, AEMHs, such as SrCl₂, possess an unparalleled NH₃ uptake capacity (approximately 50 mmol/g) due to the chemisorption mechanism, which leads to metal amine complex formation [13,14]. The AEMHs, such as SrCl₂, can store more H₂ than NH₃ in a given volume due to the higher packing density of NH₃ in the AEMHs than that of liquid NH₃ [19]. For example,

* Corresponding author.

** Corresponding author.

E-mail addresses: zhejian@chalmers.se (Z. Cao), farid.akhtar@ltu.se (F. Akhtar).

<https://doi.org/10.1016/j.ijhydene.2025.04.432>

Received 6 February 2025; Received in revised form 9 April 2025; Accepted 25 April 2025

Available online 3 May 2025

0360-3199/© 2025 The Authors. Published by Elsevier Ltd on behalf of Hydrogen Energy Publications LLC. This is an open access article under the CC BY license (<http://creativecommons.org/licenses/by/4.0/>).

1 mol of SrCl₂ can store 8 mol of NH₃, as shown in equation (1) [13,14]. These materials have been used in adsorptive NH₃ refrigeration and chemical heat pump systems where the AEMHs coating is applied over a metallic structure [20]. These materials can be easily regenerated by applying a vacuum with a mild temperature. For practical applications, the AEMHs need to be structured into appropriate shapes and geometries to ensure efficient mass and heat transport characteristics. There have been efforts to fabricate pellets of the AEMHs, but the structure disintegrated during the NH₃ sorption cycles due to volumetric expansion [21]. The volumetric expansion destroys the fabricated structures, affecting the process efficiency and poses a severe safety risk. Therefore, various approaches have been considered to manufacture stable structures that can tolerate the volumetric changes during NH₃ sorption.



Recently, efforts have yielded significant positive outcomes in terms of stability, mass, and heat transport, resulting in stable and reusable sorbents. The NH₃ sorption over AEMHs exhibits sluggish kinetics attributed to the low ammonia diffusivity in halides, which has reportedly been improved by incorporating carbon materials such as graphite, carbon nanotubes, and graphene. Recently, our group reported the structuring of MgCl₂ composites reinforced with graphite and graphene nanoplatelets, demonstrating good stability and reduced deformation problem [21]. Later, our group reported a stable, reusable, and optimized porous structure of SrCl₂ scaffolded by graphene fabricated through freeze drying. The structured sorbents demonstrated resilience against the volume changes with significant improvement in the NH₃ sorption kinetic, particularly the time to reach saturation capacity was reduced from 92 min for SrCl₂ to 27 min for the designed composite [13]. Although suitable for manufacturing simple structures, the freeze-drying process is laborious and challenging to design and scale up for complex geometries with lower pressure drops and higher mass transfer [22]. In this work, we designed and fabricated SrCl₂ structures using advanced 3D printing technologies, which have the potential to produce complex structures that offer better gas diffusion and accommodate volume expansion by breathing space in the channels. Besides the fabrication technique, the stability and strength of the structure are primarily governed by the characteristics of the binder used in the additive manufacturing process. Organic binders, such as polyvinylpyrrolidone (PVP), which have a relatively low melting point and poor thermal stability, may not be suitable for AEMHs sorbents aimed at NH₃ storage due to the release of large amounts of heat during chemisorption. An alternative option is to use inorganic binders, such as clay, silica, and bentonite, which offer high thermal stability and mechanical strength. This study reports the fabrication of SrCl₂ monolith structures using bentonite as a binder via direct ink writing (DIW), an extrusion-based 3D printing technique. Different structures were printed by varying the loading of SrCl₂ and bentonite. The fabricated monoliths were characterized using various techniques and evaluated for NH₃ sorption. Additionally, the NH₃ sorption kinetics were investigated using pseudo-first-order and pseudo-second-order models. High-pressure isotherms were recorded and explained by the dual-site Langmuir-Freundlich model, indicating surface heterogeneity in terms of energies and binding sites for NH₃ sorption.

2. Experimental

2.1. Fabrication of 3D-printed SrCl₂ monoliths

Strontium chloride (anhydrous, 99.9 % purity, Sigma Aldrich, USA) and Na-bentonite (ClearOFF Minerals, UK) were mixed and milled in a ball mill (Pulverisette 6, Fritsch, Germany) at varying mass ratios to achieve a finely dispersed powder with a particle size below 63 μm. The salt tends to form agglomerates when mixed with water due to its high hygroscopicity, which can clog the nozzle, hindering the ink's printability. Therefore, the powder underwent a controlled hydration step in

a 90 % relative humidity (R.H.) chamber for 72 h prior to ink preparation. The powder and distilled water were mixed on a high-energy planetary mixer (ARE250, The Thinky Corporation, Japan) for 15 min at 2000 rpm. Table 1 reports an overview of the composition of the three slurries examined. Before loading the ink into the syringe, sonication was performed for 15 min to enhance homogeneity. The resulting ink was loaded into a syringe (Vieweg GmbH, Germany) and printed with a 0.41 mm diameter nozzle (Vieweg GmbH, Germany). The scaffolds were 3D-printed using a Delta Wasp 2040 Turbo printer (WASP, Italy) equipped with a pneumatic extruder at a feed rate of 15 mm/s, 2.5 bar, and room temperature; PTFE sheets were used as substrate to facilitate later removal. Subsequently, the printed samples were placed in a static oven set at 40 °C for 48 h to ensure thorough drying. The dimensions of the printed cylindrical lattices were 9.5 mm in diameter and 4 mm in height. Notably, considering the solubility of the hexahydrate salt of 150 g/L at room temperature, all compositions yielded strongly super-saturated slurries.

2.2. Characterization methods

The 3D-printed monoliths were characterized using different analytical techniques to evaluate their physical and chemical properties. The microstructure of the samples was investigated using scanning electron microscopy with energy-dispersive X-ray spectroscopy (SEM, JSM-IT300, JEOL, Japan). The crystallinity of the samples was evaluated using CuKα radiations on an X-ray diffractometer (PANalytical Empyrean X-ray diffractometer, Malvern, UK) with a step size of 0.02° and scan speed of 1.2°/min operating at current and voltage of 40 mA and 45 kV, respectively (samples were dried at 150 °C before the XRD analysis). Thermal behavior was estimated by thermogravimetric analysis equipped with differential scanning calorimetry (TGA/DSC, SDT 650, TA instruments, USA) with a 10 °C/min ramping rate under an argon (Ar) gas environment. Surface area and pore size were evaluated using a surface analyzer (Micromeritics® ASAP 2020 Plus, USA) with nitrogen sorption and desorption at a temperature of −196 °C. Before analysis, the samples were degassed overnight at 150 °C under vacuum conditions. BET surface area was measured from a linear range by selecting the relative pressure (P/P₀) of 0.01–0.1. The mechanical properties of the porous structures were evaluated under uniaxial compression using a universal testing machine (Quasar 25, Galdabini, Italy) with 0.5 mm/min cross-head speed. For each composition, at least 10 specimens underwent testing, generating survival probability curves under uniform compression conditions according to the Weibull method.

2.3. NH₃ sorption-desorption experiments

The NH₃ sorption and desorption experiments were conducted using the IsoSORP sorption analyzer (High-pressure TGA, TA instrument, New Castle, DE, USA), as reported in our previous study [18]. Structured samples were directly loaded into the sorption chamber. Before every measurement, samples were degassed at 150 °C under a vacuum for 3 h. A buoyancy measurement was conducted to estimate the mass and volume of the sample using helium gas (99.99 % purity) at a pressure of 10 bar and a temperature of 20 °C. After that, NH₃ sorption experiments were performed at 3 bar and 20 °C, and desorption was carried out under vacuum at the same temperature. Screening and cycling measurements both were carried out under identical conditions. Thermal regeneration under vacuum was performed between cycles during cycling

Table 1
Compositions for the SrCl₂-bentonite slurries.

SrCl ₂ (wt.%) to Na-bentonite (wt.%)	Salt-to-water mass ratio
60–40	1.03
70–30	1.27
80–20	1.37

measurements.

Sorption and desorption isotherms were recorded starting in the 0–3 bar range at different temperatures of 20, 30, and 40 °C, respectively. During the recording of isotherms, the temperature was controlled by the oil bath circulation system. Additionally, kinetic experiments were conducted using a thermal analyzer (TGA/DSC, SDT 650, TA Instruments, USA). Samples were degassed for 2 h at 150 °C, followed by cooling to room temperature using an argon gas environment. After cooling, the gas was switched to NH₃, and sorption curves were recorded. The duration of the experiment was determined based on changes in the sample mass during NH₃ sorption, and measurements were stopped when no further change in mass occurred over time.

3. Results and discussion

3.1. 3D-printed SrCl₂ monoliths

SEM images were acquired to investigate the microstructure of the optimized 3D 60 % SrCl₂ monoliths before and after ammonia sorption-desorption cycles, as shown in Fig. 1. The obtained 3D-printed structures consisted of in-layer parallel stripes with a width of ~350 μm and a gap width of ~400 μm. Stripes were oriented perpendicular to those of adjacent layers to create a sieve-like 3D structure. The designed sieve-like structures with channels provided ample free space, which could potentially enhance gas transportation and accommodate volumetric changes during NH₃ sorption. For the zoomed-in SEM images and their corresponding EDX mapping, we observed that SrCl₂ agglomerates were surrounded by bentonite, suggesting that bentonite provided mechanical support for SrCl₂ to hold the printed structure. The agglomeration of SrCl₂ was observed in 3D 70 % SrCl₂ and 3D 80 % SrCl₂ structures as well, as shown in Fig. S1. After cyclic measurements, local disintegration was found on the SrCl₂ agglomerates, as shown in Fig. 1 (c), which was attributed to the volumetric expansion and shrinkage during the NH₃ sorption and desorption [23].

The crystallinity of 3D-printed structures and individual components was measured using XRD analysis, as shown in Fig. 2 (a). The prominent peaks at 2θ values of 22°, 36°, and 43° represented the presence of SrCl₂.

Meanwhile, the reference diffractogram of bentonite shows the peaks at 9, 20°, 27°, and 35°, corresponding to basal planes of sodium bentonite, respectively [24]. However, no peak was observed for bentonite in the 3D-printed structure, possibly due to the intercalation of a higher concentration of SrCl₂ in the bentonite layers, which may lead to the exfoliation of the bentonite layers and, thus, result in a significantly broadened d-spacing. Block et al. reported the broadening and diminished XRD peaks with the loading of peptides over montmorillonite (MMT) due to intercalation and exfoliation [25]. Higher loading of bentonite could shift the peaks to lower angles, and also, peaks might have been shielded by strong peaks of SrCl₂ [26]. Similarly, Choudary et al. reported that with increased concentration of MMT clay, the exfoliated and intercalated MMT showed no peaks in the XRD diffractogram [27].

Fig. 2 (b and c) shows the TGA/DSC curves of 3D-printed structures, bentonite, and SrCl₂. The TGA curves show the weight loss at different temperature regimes. The weight loss below 200 °C resulted from the removal of surface adsorbed water and other gaseous substances [28]. The SrCl₂ powder exhibited comparatively lower weight loss than bentonite and bentonite-containing samples. Generally, loosely bonded water molecules between the bentonite layers are stripped off during heating at low temperatures. Unlike bentonite, SrCl₂ did not present significant amounts of weakly bonded water molecules. Weight loss below 200 °C could result from the adsorbed water molecules and detachment of bounded moisture in the bentonite and SrCl₂ [28,29]. The bentonite underwent a phase transformation from 500 °C to 700 °C, as indicated by the endothermic peak in the DSC curve in Fig. 2 (c). The irreversible dehydroxylation of the bentonite lattice occurs at temperatures above 500 °C, which may affect the porous scaffolding by reducing pore volume and sorption capacity [30]. To avoid phase transformation and distortion of the porous structure, the 3D-printed samples were not subjected to high-temperature heat treatment.

To analyze the surface area and pore size characteristics, the N₂ sorption isotherms for different samples were recorded, as shown in Fig. 2 (d). SrCl₂ showed type II isotherm, indicating macroporous or nonporous structure according to the classification by the International Union of Pure and Applied Chemistry (IUPAC) [31,32]. The reference

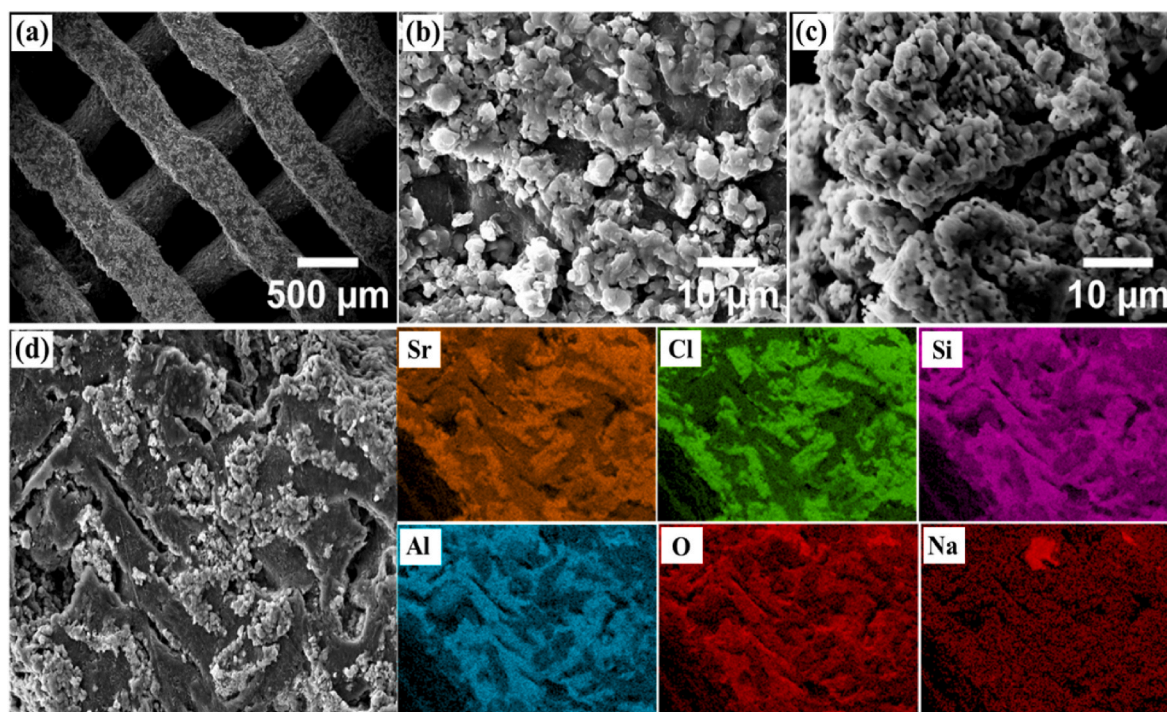


Fig. 1. SEM micrographs of 3D 60 % SrCl₂: (a, b) As-printed sample, (c) After NH₃ sorption, and (d) EDX elemental mapping of the as-printed sample.

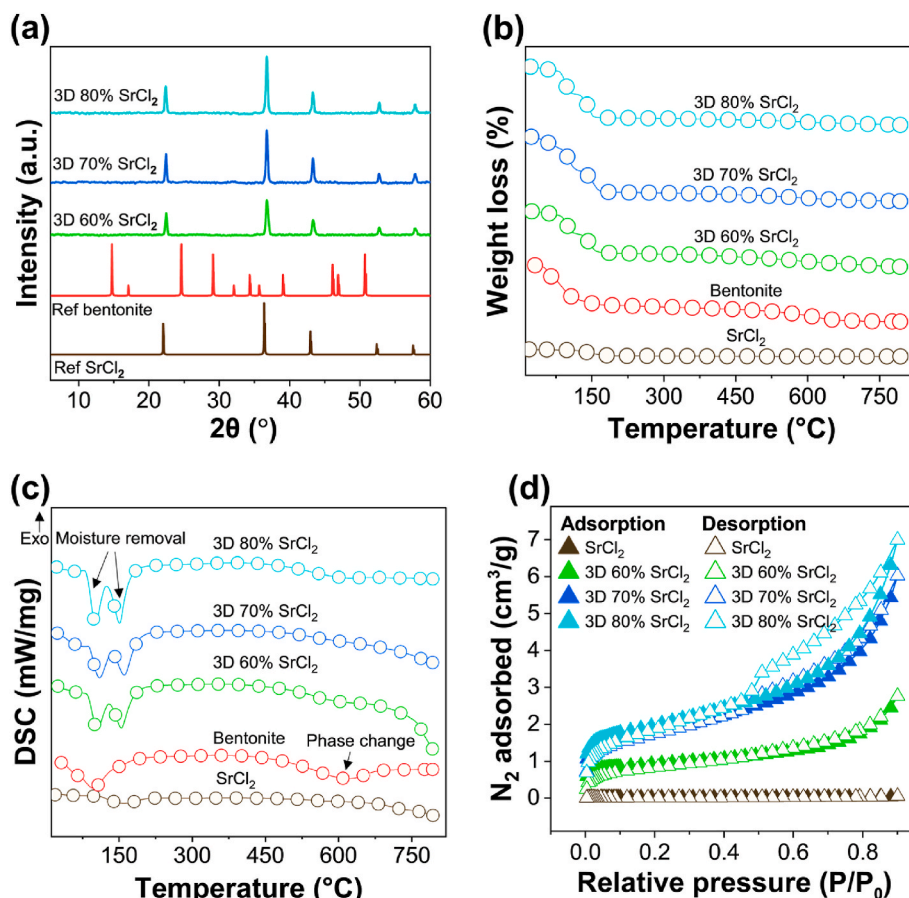


Fig. 2. Characterizations of 3D-printed samples: (a) XRD patterns, (b, c) TGA and DSC thermal stability plots, and (d) N₂ adsorption and desorption isotherms.

bentonite sample exhibited a type IV isotherm with a hysteresis loop, as shown in Fig. S2, indicating the characteristic behavior of a mesoporous material. Hysteresis shown by the bentonite is a type H3, typical of a slit-like pore geometry. Furthermore, adsorption at $P/P_0 < 0.05$ indicated the presence of micropores. The surface area of bentonite was 55 m²/g, substantially greater than SrCl₂. The 3D-printed samples exhibited moderate specific surface area values compared to bentonite and SrCl₂ with 3, 6, and 7 m²/g corresponding to 60, 70, and 80 % SrCl₂ loading, respectively. In all cases, considering a negligible contribution from SrCl₂, the values are lower than what is expected from rule-of-mixtures calculations, indicating some extent of pore filling or occlusion due to the crystallization of the salt. Notably, the sample with the lowest fraction of bentonite displays its intrinsic pore structure more clearly, as seen from the presence of the hysteresis loop, which is instead less evident at 30 % and completely absent in the samples at 40 %; as a result, the SSA counterintuitively increases with decreasing fractions of bentonite. The reasons for this phenomenon may be related to the different concentrations of SrCl₂ with respect to water in the three slurries, which increases with fractions of SrCl₂. As shown in Table 1, the slurry used to prepare the 80 % SrCl₂ composites presents the highest supersaturation, likely resulting in a more viscous liquid phase and preventing significant penetration into the mesoporous network of the bentonite. This is supported by the low discrepancy between the measured (7 m²/g) and expected (≈ 11 m²/g) values for the 3D 80 % SrCl₂ sample. In contrast, as the salt/water ratio is lowered, more pervasive intrusion of the liquid phase and subsequent crystallization of the salt may result in more severe damage to the intrinsic pore network of the bentonite, leading to lower SSA values (6 and 3 m²/g for 70 % and 60 % SrCl₂ respectively) and significantly more significant discrepancies with expected values (≈ 16 and ≈ 22 m²/g respectively). Nevertheless,

the addition of bentonite overall increased the surface area, pore size, and pore volume of the 3D-printed samples compared to pure SrCl₂, which would be beneficial for the mass transport of NH₃ molecules through the printed structure.

Despite notable variations observed in the mechanical responses of individual scaffolds within each composition, a consistent pattern emerged in all compression tests, as shown in Fig. 3. In fact, samples displayed a typical sequence. Each test had an initial region characterized by a slight increase in stress with rising compressive strain. Subsequently, a region of linear elastic deformation ensued before discontinuities appeared above a stress threshold, varying for each scaffold. These discontinuities indicated internal subcritical fractures of individual struts, which preceded the attainment of peak load and ultimate structural collapse. Similar to the behavior of many cellular structures, a distinctive plateau region with a constant crushing strength was observed after the peak load [33]. The 80 % composition exhibited a Weibull modulus (m) of 1.94 and the lowest scale factor (σ) at 0.26 MPa among all compositions. This composition demonstrated the lowest performance, with compression stresses varying narrowly between 0.1 and 0.5 MPa. Evaluation of mechanical data was challenging due to structures failing at very low stress levels, making fracture indications less evident in the stress curves. For the 70 % composition, the specimen consistently failed at approximately the same compression stress, around 1–1.5 MPa, suggesting a more homogeneous structure of the monoliths. This composition exhibited a Weibull modulus (m) of 2.17, indicative of enhanced material consistency. A higher Weibull modulus implies more evenly distributed defects throughout the entire volume and a narrower probability distribution curve for the strength. The calculated scale factor was 2.59 MPa. Lastly, for the 60 % composition, the Weibull modulus (m) increased to 2.58, accompanied by a scale

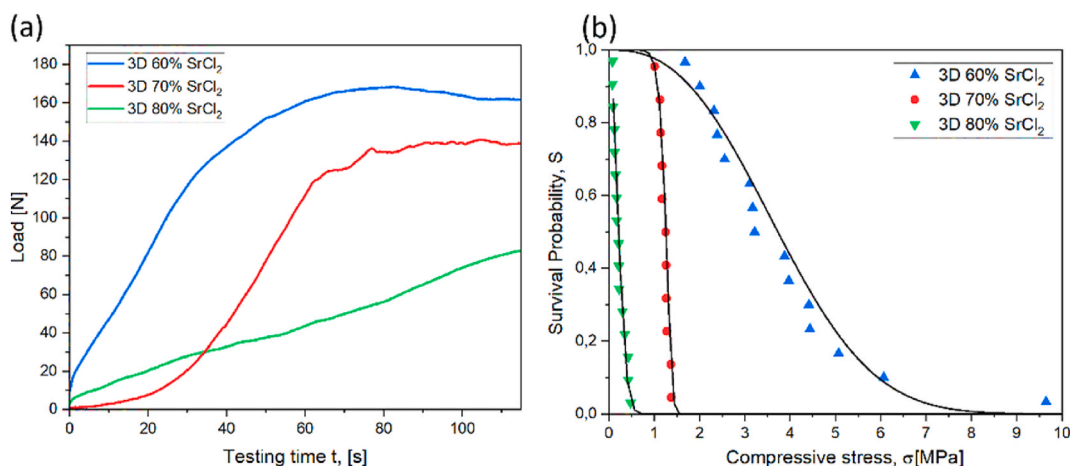


Fig. 3. (a) Representative mechanical behavior in compression for 3D-printed samples, and (b) corresponding survival probability data. Solid curves in (b) indicate calculated survival probability curves obtained through the Weibull approximation.

factor (σ) of 4.3 MPa. As the tested population increased, a broader range of compression stresses, reaching up to 10 MPa, was observed. Minimum fracture stresses also rose to approximately 2 MPa, indicating a considerable enhancement in mechanical performance with higher bentonite content. Overall, the compressive strength of SrCl₂-bentonite increased with the addition of bentonite by reducing the content of SrCl₂. Despite not being subjected to any thermal treatment that promotes densification and sintering, bentonite builds up the structural skeleton through its many weak bonds. Moreover, its beneficial effect of improved slurry rheology results in a more homogeneous cell structure with fewer defects that might initiate fractures.

3.2. NH₃ sorption-desorption performance

The sorption performance of the obtained specimens was

characterized by their ammonia uptake capacity and kinetics, as shown in Fig. 4 (a). It is evident that the NH₃ sorption capacity increased proportionally to the loading of SrCl₂, with the highest sorption capacity of 842 mg/g (49.53 mmol/g) achieved by the pristine SrCl₂ powder. The sorption capacity of the 3D-printed samples was 488, 572, and 644 mg/g, corresponding to compositions of 60, 70, and 80 % loading, respectively. This indicates that SrCl₂ was the primary active component for NH₃ sorption [34]. Meanwhile, the bentonite exhibited an NH₃ uptake of 63 mg/g (5 mmol/g), which was approximately ten times lower than that of SrCl₂ due to physisorption rather than chemisorption.

The sorption kinetics plots, with normalized NH₃ uptake capacity (percentage) corresponding to the saturation capacity of each sorbent, are shown in Fig. 4 (b). The equilibrium pressure estimated from the Van't Hoff equation at 20 °C was 0.47 bar; thus, the duration of the adsorption and desorption period was calculated from this point to

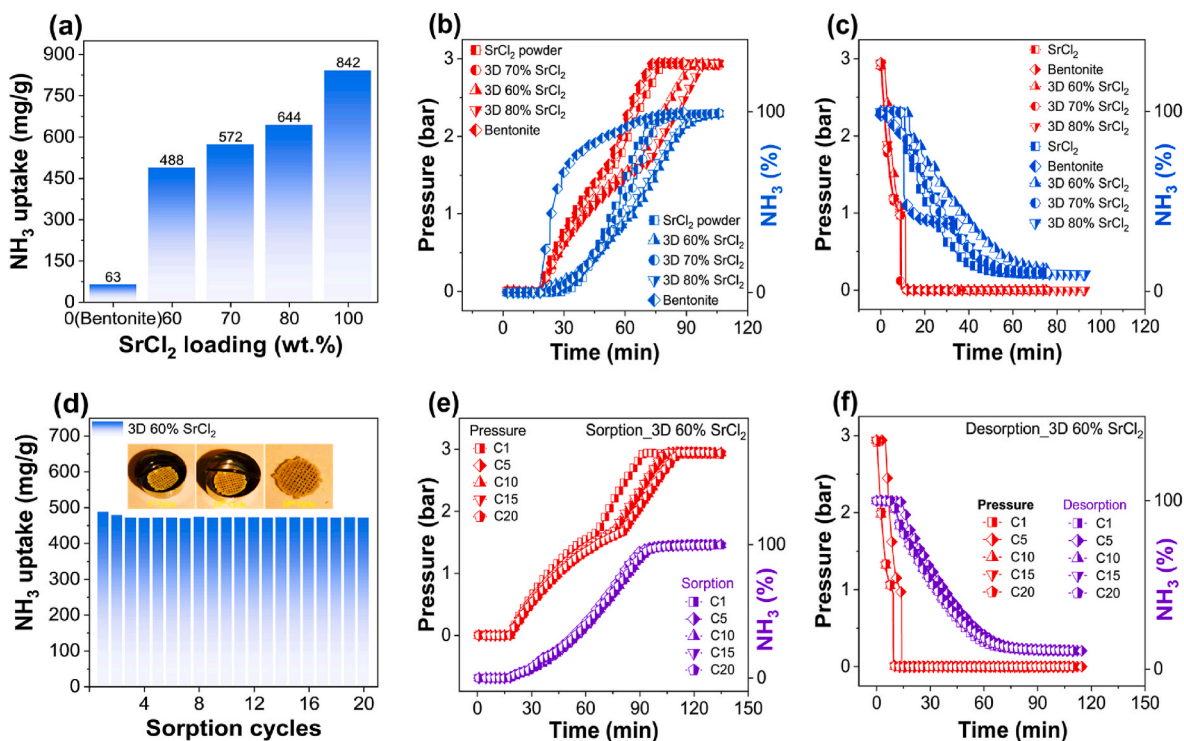


Fig. 4. (a) NH₃ uptake capacity, (b) Sorption kinetics, (c) Desorption kinetics, (d) 20 cycles of NH₃ uptake of 3D 60 % SrCl₂, with photos of the structure after 1, 10, and 20 cycles, (e) Sorption kinetics, and (d) Desorption kinetics of cyclic measurements for 3D 60 % SrCl₂ sample.

saturation for SrCl₂ [13]. Bentonite reached 70 % of its saturation capacity within 30 min at 1.5 bar and showed maximum adsorption at low pressure. This confirmed the physical adsorption from bentonite, which was faster than the chemisorption reaction between the SrCl₂ and NH₃. Meanwhile, pristine SrCl₂ showed an insignificant capacity at pressures below 0.47 bar, whereas the 3D-printed samples demonstrated the contribution of bentonite at low pressures, making them superior sorbents for low-pressure NH₃ sorption applications. Although there was a contribution from physical adsorption, the primary NH₃ uptake originated from the chemisorption owing to the amine complex (Sr (NH₃)₈Cl₂). The time to reach saturation capacity for SrCl₂ powder was 82 min, whereas 3D-printed samples reached saturation capacity in 106, 96, and 96 min for 60, 70, and 80 % loading, respectively. This shows that the sorption kinetics of 3D-printed samples were slower than pristine SrCl₂ powder. Since the metal-amine complex formation using SrCl₂ is an exothermic reaction [34], the removal or transfer of heat of the reaction plays a crucial role. The bentonite could decelerate the sorption kinetics due to its poor thermal transport properties, leading to increased local temperatures within the sample, which could decrease the rate of the exothermic reaction of metal-amine complex formation. As seen in SEM images (Fig. 1), larger agglomerate size could increase diffusion length, further slowing the sorption kinetics. Adsorption usually starts on the surface and then diffuses into the bulk. Therefore, the available surface area is crucial in attaching the NH₃ molecules to SrCl₂. This also explains that the 3D 70 % SrCl₂ and 3D 80 % SrCl₂ presented rapid kinetics due to their higher specific surface area (SSA) compared to the 3D 60 % SrCl₂. Fig. 4 (c) shows the desorption profile of the 3D-printed samples, where the desorption pattern followed a trend similar to that of adsorption regarding the time to regenerate the samples.

Cyclic NH₃ sorption experiments were conducted for different 3D-printed samples. Fig. S3 shows the NH₃ sorption of consecutive 10 cycles for sample 3D 70 % SrCl₂. The sample remained stable after the first cycle, with no visible cracks or loose particles observed within the reaction chamber. After the 3rd cycle, a crack appeared from the center of the monolith, both on the top and bottom sides. The crack propagated more with subsequent cycles, and the structure fractured into two parts after the 5th cycle. The development of cracks and breakage during cyclic measurements shows how expansion and contraction during NH₃ sorption affect the mechanical stability of the structure. Interestingly, after the 5th cycle, structured sorbents did not undergo further disintegration up to the 10th cycle. However, there were some loose particles in the chamber, indicating the progressive degradation. The sorption and desorption kinetics of the 3D 70 % SrCl₂ followed almost identical pattern, as shown in Fig. S4. Similarly, the 3D 80 % SrCl₂ sample was evaluated for cyclic adsorption, and the structure fractured after the second cycle, indicating that volumetric expansion destroyed the structure due to its decreased mechanical performance, as shown in Fig. S5. Furthermore, the NH₃ uptake of the 3D 60 % SrCl₂ sample was evaluated over 20 consecutive cycles, as shown in Fig. 4 (d). The sample exhibited stable NH₃ sorption performance, with no change in sorption capacity over time. The structure of the sample remained intact, with no apparent cracks or breakage, as shown in the photo in Fig. 4 (d), indicating that there were sufficient free open channels in the structure to accommodate the volumetric expansion effectively. This indicates that bentonite, as a binder, effectively retained SrCl₂ within the structure, preventing further disintegration due to volume expansion. Adsorption and desorption kinetics for cyclic measurements are plotted in Fig. 4 (e and f), and the time for cyclic adsorption and desorption kinetics is shown in Table S1. The saturation time for cyclic measurements was almost identical, with slight variations. As shown in the SEM image (Fig. 1 (c)), pores generation due to NH₃ sorption and desorption could have slightly improved the kinetics.

3.3. Kinetic study

The high-pressure NH₃ isotherms were recorded at different temperatures (20, 30, and 40 °C) for 3D-printed samples to understand the adsorption of NH₃ molecules, as shown in Fig. 5 (a–c). As expected, there was negligible adsorption in the low-pressure region (<0.4 bar) due to the limitation of SrCl₂, and sorption capacity sharply increased after passing the threshold equilibrium pressure [35]. The 3D 60 % SrCl₂ sample at 20 °C and 1 bar pressure reaches almost 94 % of the saturation capacity. Meanwhile, the sorption capacity was susceptible to temperature changes due to the exothermic nature of the metal-amine complex reaction, which is the dominant sorption mechanism in NH₃ storage using AEMHs. The 3D 60 % SrCl₂ sample exhibited only 14 % and 10.5 % of the saturation capacities at 30 and 40 °C, respectively. This shows the significant decrease in sorption over SrCl₂ with temperature. On the other hand, at high pressures, especially >1.5 bar, there was no significant difference in the sorption capacity with temperature. At 3 bar pressure, the difference in sorption capacity between 20 and 30 °C was approximately 8 %, indicating that the metal amine complex reaction proceeds rapidly at high pressure. The decreased sorption capacity can be ascribed to the exothermic chemisorption reaction and decrease in the forces responsible for the physical attachment of NH₃ molecules to the surface of 3D-printed structures [36]. There is clear hysteresis due to very low desorption at higher-pressure regions, which has been reported for AEMHs, indicating that reduction in pressure does not fully facilitate the bond cleavage in the metal-amine complex. None of the sorbents was fully regenerated under vacuum owing to the strong binding of the monoamine phase (SrCl₂·NH₃). Regeneration of the monoamine phase needed thermal treatment to fully regenerate the sorbent to the original sorption capacity.

As shown in Fig. 5 (d–f), adsorption isotherms data fitted with the dual-site Langmuir-Freundlich model following equation (2) [37]:

$$Qe = Q_{max1} \frac{b_1 P^{n_1}}{1 + b_1 P^{n_1}} + Q_{max2} \frac{b_2 P^{n_2}}{1 + b_2 P^{n_2}} \quad (2)$$

where Q_{max} is the maximum sorbent capacity, b describes the adsorbate-adsorbent affinity, and n represents the surface heterogeneity and adsorption intensity. A value of $n > 1$ shows the cooperative adsorption over the sorbent [38]. The surface heterogeneity may arise from different sorption mechanisms, such as surface sites with physical and chemical potential. The structures comprise physical adsorption sites due to bentonite and chemical adsorption sites due to SrCl₂, as well as the energy difference between the heat of formation of the monoamine and the octaamine phase for metal-amine complex formation. The mono-amine phase is considered the stronger bond compared to the octa-amine phase, thus having higher binding energy [39]. It is worth noting that adsorption proceeding through metal-amine complex formation strongly depends on the pressure but shows close values at higher-pressure regions regardless of temperature [40]. The values of the n were 68.39, 4.29, and 2.45, corresponding to 60, 70 and 80 % loading of SrCl₂ in the 3D-printed structures. Higher values of n indicated a higher surface affinity, resulting in more cooperative adsorption. Although model fitting using dual site Langmuir-Freundlich predicted the surface heterogeneity and energy distribution, it cannot give exact values and capacity of each site.

In addition, gas adsorption in a solid can be limited due to mass transfer resistance, primarily the diffusion of the sorbate within the sorbent, which could be intercrystalline or intracrystalline, depending on the material characteristics and the sorption mechanism. The model fitting was performed to evaluate the diffusion parameters and estimate the rate-controlling factors. Intercrystalline and intracrystalline diffusion models were validated using random walk model equation (3) [41]:

$$\ln \left(1 - \frac{m}{m_{\infty}} \right) = \ln \left(\frac{6}{R} \right) - \frac{\pi^2 D t}{R^2} \quad (3)$$

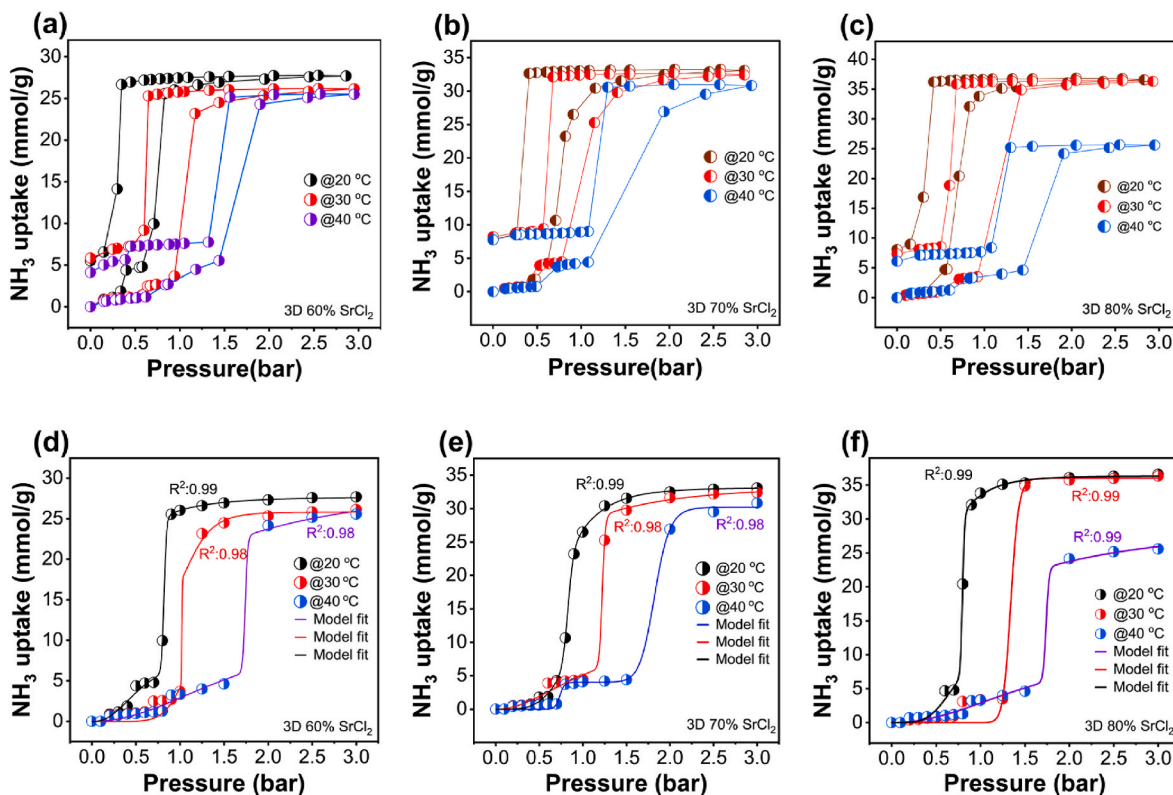


Fig. 5. (a, b, c) NH_3 sorption isotherms and (d, e, f) dual site Langmuir-Freundlich model fitting for 3D-printed samples.

where R is half of the diagonal distance of the salt crystal, D represents the diffusion coefficient, and t is the time. The values of $\frac{m}{m_\infty} < 0.5$ were used for the intracrystalline diffusion and $\frac{m}{m_\infty} > 0.75$ was used for the

intercrystalline diffusion [41,42]. As shown in Fig. 6 (a–c), the intercrystalline diffusion model provided a good fit for the 3D-printed samples. As salts are either macroporous or nonporous materials without micropores, the primary controlling factor may be the diffusion of NH_3

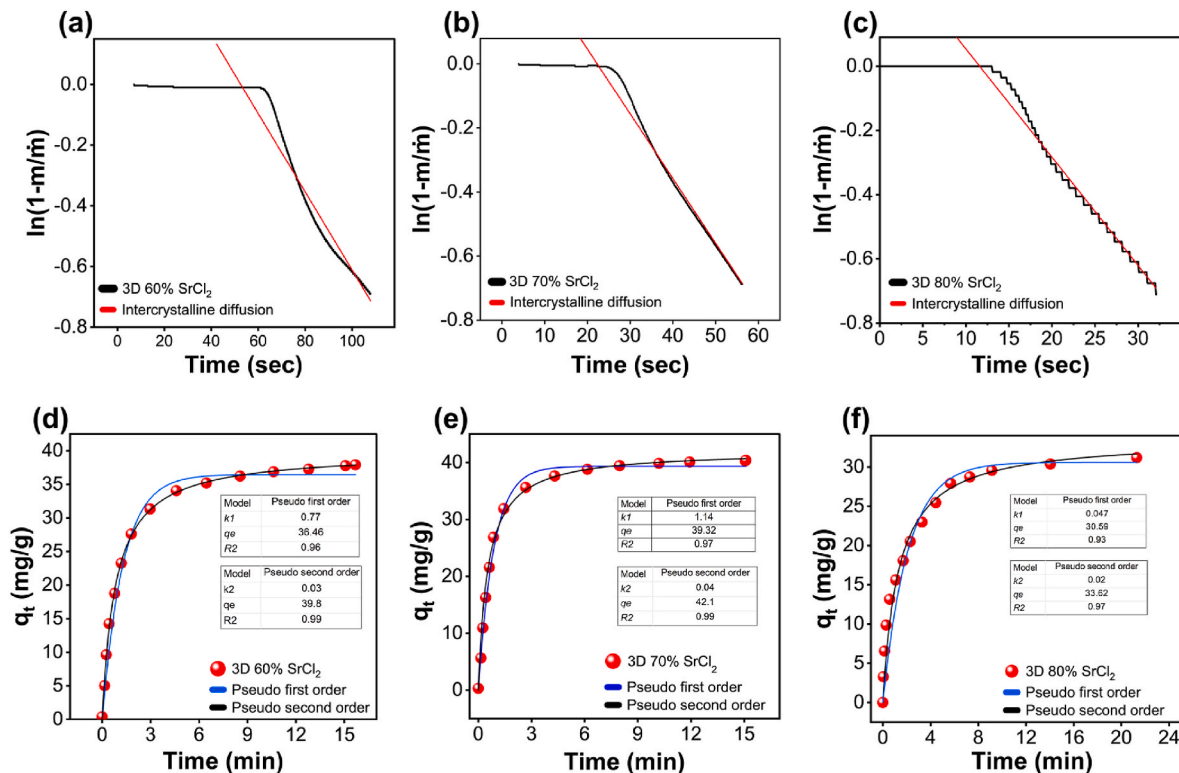


Fig. 6. (a, b, c) Diffusion models fitting, and (d, e, f) reaction kinetic models fitting for 3D-printed samples.

molecules through the macropores between particles. The intracrystalline diffusion model exhibited relatively poor fitting, as illustrated in Fig. S6 (a–c), suggesting the absence of micropores diffusion dynamics. Estimated values of diffusion coefficient are 0.01, 0.02, and 0.03, corresponding to the 3D 80 % SrCl₂ > 3D 70 % SrCl₂ > 3D 60 % SrCl₂, respectively. This trend correlates with the surface area of the 3D-printed samples, suggesting that the surface area of the samples may play a critical role in controlling the mass transport of the sorbate.

In addition, reaction kinetics were estimated using pseudo-first and second-order reaction kinetics using equations (4) and (5) [39,43]:

$$q_t = q_e(1 - \exp(-k_1 t)) \quad (4)$$

$$q_t = \frac{k_2 q_e^2 t}{1 + k_2 q_e t} \quad (5)$$

where q_t is the adsorbent capacity at time t , q_e is the equilibrium capacity, and k is the rate constant. According to the values of regression coefficients, R^2 , and Fig. 6 (d–f), sorption kinetics follows the pseudo-second-order kinetics, indicating that sorption is proportional to the square of partial pressure of NH₃. These results are in line with the sorption dependency on the partial pressure of NH₃ revealed by the high-pressure isotherms, where the rate of sorption increased exponentially rather than linearly above the threshold partial pressure of NH₃. It also shows that increasing the partial pressure would be essentially beneficial for NH₃ sorption over the 3D-printed structure. In addition, the value of the rate constant was higher for 3D 80 % SrCl₂, which supports the sorption and desorption results observed in Fig. 4 (e and f), where the time to reach saturation was lower for the 80 % SrCl₂ loading. The kinetics of NH₃ chemisorption on AEMHs, through metal-amine complex formation, follow a pseudo-second-order model [39]. It is worth mentioning that pseudo-first or second-order kinetics models are not representative of either chemisorption or physisorption. These kinetic models only show the dependency of the reaction relative to the partial pressure of reactants. Inferring physical or chemical mechanisms could lead to discrepancies.

4. Conclusions

In summary, we designed and printed various SrCl₂ and bentonite structures with different salt loading using the direct ink writing method (DIW). The optimized sample, 3D 60 % SrCl₂, demonstrated excellent performance and stability over 20 consecutive cycles, effectively accommodating volumetric changes during NH₃ sorption cycles while maintaining structural integrity. The kinetics were explained by the pseudo-second-order model, which elucidated the rapid increase in NH₃ sorption after the threshold pressure. The high-pressure isotherm data fitted well with the dual-site Langmuir-Freundlich model, explaining the surface heterogeneity in terms of physical and chemical sorption originating from SrCl₂ and bentonite. The random walk model fitting verified that intercrystalline gas particle movement was the diffusion-controlling factor due to the non-porous nature of the salt. The robust and efficient 3D-printed SrCl₂ structures demonstrated significant potential for use as an ammonia carrier in various hydrogen storage applications.

CRedit authorship contribution statement

Nasir Shezad: Writing – original draft, Investigation, Funding acquisition, Formal analysis, Data curation. **Marco D’Agostini:** Writing – review & editing, Investigation, Data curation. **Ali Ezzine:** Formal analysis, Data curation. **Giorgia Franchin:** Writing – review & editing, Supervision, Investigation. **Paolo Colombo:** Writing – review & editing, Supervision, Funding acquisition. **Zhejian Cao:** Writing – review & editing, Supervision, Formal analysis, Conceptualization. **Farid Akhtar:** Writing – review & editing, Supervision, Resources, Project administration, Funding acquisition, Conceptualization.

Data availability

Data will be made available on request.

Declaration of competing interest

The authors declare that they have no known competing financial interests or personal relationships that could have appeared to influence the work reported in this paper.

Acknowledgments

This work has been supported under the National Recovery and Resilience Plan (NRRP), Mission 4 Component 2 Investment 1.4 - Call for tender No. 3138 of December 16, 2021 of the Italian Ministry of University and Research, funded by the European Union - NextGenerationEU [Award Number: CNMS named MOST, Concession Decree No. 1033 of June 17, 2022, adopted by the Italian Ministry of University and Research, Spoke 14 “Hydrogen and New Fuels”] and Vetenskapsrådet, Sweden (No. 2018–04407).

Appendix A. Supplementary data

Supplementary data to this article can be found online at <https://doi.org/10.1016/j.ijhydene.2025.04.432>.

References

- [1] Net Zero Coalition | United Nations n.d. <https://www.un.org/en/climatechange/net-zero-coalition> (accessed September 24, 2022).
- [2] Parra D, Valverde L, Pino FJ, Patel MK. A review on the role, cost and value of hydrogen energy systems for deep decarbonisation. *Renew Sustain Energy Rev* 2019;101:279–94. <https://doi.org/10.1016/j.rser.2018.11.010>.
- [3] Midilli A, Ay M, Dincer I, Rosen MA. On hydrogen and hydrogen energy strategies: I: current status and needs. *Renew Sustain Energy Rev* 2005;9:255–71. <https://doi.org/10.1016/j.rser.2004.05.003>.
- [4] Yue M, Lambert H, Pahon E, Roche R, Jemei S, Hissel D. Hydrogen energy systems: a critical review of technologies, applications, trends and challenges. *Renew Sustain Energy Rev* 2021;146. <https://doi.org/10.1016/j.rser.2021.111180>.
- [5] Abe JO, Popoola API, Ajenifuja E, Popoola OM. Hydrogen energy, economy and storage: review and recommendation. *Int J Hydrogen Energy* 2019;44:15072–86. <https://doi.org/10.1016/j.ijhydene.2019.04.068>.
- [6] Lu X, Krutoff AC, Wappler M, Fischer A. Key influencing factors on hydrogen storage and transportation costs: a systematic literature review. *Int J Hydrogen Energy* 2025;105:308–25. <https://doi.org/10.1016/j.ijhydene.2025.01.196>.
- [7] Salehabadi A, Perry J, Zanganeh J, Moghtaderi B. Emerging perovskite-based catalysts for sustainable and green ammonia production: a promising hydrogen energy carrier. *Int J Hydrogen Energy* 2025;106:243–60. <https://doi.org/10.1016/j.ijhydene.2025.01.283>.
- [8] Sun B, Chen Y, Zhang G, Ni S, Li C, Li X. Research on in situ formed TiH₂ and Mg₂Ni for the hydrogen storage performance of Mg₉₉Ni₁₀-Ti. *Int J Hydrogen Energy* 2025;101:582–93. <https://doi.org/10.1016/j.ijhydene.2024.12.471>.
- [9] Liu B, Xu L, Xu Y, Wang K, Kang Z, She X. Optimizing ammonia decomposition for hydrogen production via segmented electric heating. *Int J Hydrogen Energy* 2025;103:480–90. <https://doi.org/10.1016/j.ijhydene.2024.12.482>.
- [10] Makepeace JW, He T, Weidenthaler C, Jensen TR, Chang F, Vegge T, et al. Reversible ammonia-based and liquid organic hydrogen carriers for high-density hydrogen storage: recent progress. *Int J Hydrogen Energy* 2019;44:7746–67. <https://doi.org/10.1016/j.ijhydene.2019.01.144>.
- [11] Anhydrous ammonia: managing the risks | NDSU agriculture and extension n.d. <https://www.ndsu.edu/agriculture/ag-hub/publications/anhydrous-ammonia-managing-risks>. [Accessed 24 September 2022].
- [12] Chatterjee S, Parsapur RK, Huang KW. Limitations of ammonia as a hydrogen energy carrier for the transportation sector. *ACS Energy Lett* 2021;6:4390–4. <https://doi.org/10.1021/acscenergylett.1c02189>.
- [13] Cao Z, Akhtar F. Porous strontium chloride scaffolded by graphene networks as ammonia carriers. *Adv Funct Mater* 2021;31. <https://doi.org/10.1002/adfm.202008505>.
- [14] Cao Zhejian, Narang Kritika, Akhtar F. Rapid ammonia carriers for SCR systems using MOFs [M₂(adc)₂ (dabco)] (M = Co, Ni, Cu, Zn). *Catalysts* 2020;2:1444. <https://doi.org/10.3390/catal10121444>.
- [15] Khabzina Y, Farrusseng D. Unravelling ammonia adsorption mechanisms of adsorbents in humid conditions. *Microporous Mesoporous Mater* 2018;265:143–8. <https://doi.org/10.1016/j.micromeso.2018.02.011>.
- [16] Rodrigues CC, de Moraes D, da Nóbrega SW, Barboza MG. Ammonia adsorption in a fixed bed of activated carbon. *Bioresour Technol* 2007;98:886–91. <https://doi.org/10.1016/j.biortech.2006.03.024>.

- [17] Saha D, Deng S. Ammonia adsorption and its effects on framework stability of MOF-5 and MOF-177. *J Colloid Interface Sci* 2010;348:615–20. <https://doi.org/10.1016/j.jcis.2010.04.078>.
- [18] Shezad N, D'Agostini M, Ezzine A, Franchin G, Colombo P, Akhtar F. 3D-printed zeolite 13X-Strontium chloride units as ammonia carriers. *Heliyon* 2023;9:e19376. <https://doi.org/10.1016/j.heliyon.2023.e19376>.
- [19] Klerke A, Christensen CH, Nørskov JK, Vegge T. Ammonia for hydrogen storage: challenges and opportunities. *J Mater Chem* 2008;18:2304–10. <https://doi.org/10.1039/b720020j>.
- [20] Capri A, Frazzica A, Calabrese L. Recent developments in coating technologies for adsorption heat pumps: a review. *Coatings* 2020;10:855. <https://doi.org/10.3390/COATINGS10090855>.
- [21] Cao Z, Grimaldos Osorio N, Cai X, Feng P, Akhtar F. Carbon-reinforced MgCl₂ composites with high structural stability as robust ammonia carriers for selective catalytic reduction system. *J Environ Chem Eng* 2020;8:103584. <https://doi.org/10.1016/j.jece.2019.103584>.
- [22] Sun K, Li R, Jiang W, Sun Y, Li H. Comparison of three-dimensional printing and vacuum freeze-dried techniques for fabricating composite scaffolds. *Biochem Biophys Res Commun* 2016;477:1085–91. <https://doi.org/10.1016/j.bbrc.2016.07.050>.
- [23] Hummelshøj JS, Sørensen RZ, Kustova MY, Johannessen T, Nørskov JK, Christensen CH. Generation of nanopores during desorption of NH₃ from Mg(NH₂)₆Cl₂. *J Am Chem Soc* 2006;128:16–7. <https://doi.org/10.1021/ja0556070>.
- [24] Alcázar-Vara LA, Guerrero-Hernández J, Chacon C, Cortés-Monroy IR. Thermal degradation kinetics and structural characterization of sodium bentonite. *Energy Sources, Part A Recovery, Util Environ Eff* 2021;16:1–14. <https://doi.org/10.1080/15567036.2021.1977871>.
- [25] Block KA, Trusiak A, Katz A, Alimova A, Wei H, Gottlieb P, et al. Exfoliation and intercalation of montmorillonite by small peptides. *Appl Clay Sci* 2015;107:173–81. <https://doi.org/10.1016/j.clay.2015.01.021>.
- [26] Lang W, Yang Q, Song X, Yin M, Zhou L. Cu nanoparticles immobilized on montmorillonite by biquaternary ammonium salts: a highly active and stable heterogeneous catalyst for cascade sequence to indole-2-carboxylic esters. *RSC Adv* 2017;7:13754–9. <https://doi.org/10.1039/c6ra25861a>.
- [27] Choudhary S, Sengwa RJ. Intercalated clay structures and amorphous behavior of solution cast and melt pressed poly(ethylene oxide)-clay nanocomposites. *J Appl Polym Sci* 2014;4:131. <https://doi.org/10.1002/app.39898>.
- [28] Clark RJ, Farid M. Experimental investigation into the performance of novel SrCl₂-based composite material for thermochemical energy storage. *J Energy Storage* 2021;36:102390. <https://doi.org/10.1016/j.est.2021.102390>.
- [29] Sarkar M, Dana K, Ghatak S, Banerjee A. Polypropylene-clay composite prepared from Indian bentonite. *Bull Mater Sci* 2008;31:23–8. <https://doi.org/10.1007/s12034-008-0005-5>.
- [30] Hulya Noyan, Muserref Onal, Yuksel Sarikaya. The effect of heating on the surface area, porosity and surface acidity of a bentonite. *Clays Clay Miner* 2006;54:375–81. <https://doi.org/10.1346/CCMN.2006.0540308>.
- [31] Thommes M, Kaneko K, Neimark AV, Olivier JP, Rodriguez-Reinoso F, Rouquerol J, et al. Physisorption of gases, with special reference to the evaluation of surface area and pore size distribution (IUPAC Technical Report). *Pure Appl Chem* 2015;87:1051–69. <https://doi.org/10.1515/pac-2014-1117>.
- [32] Wang L, Chen L, Wang HL, Liao DL. The adsorption refrigeration characteristics of alkaline-earth metal chlorides and its composite adsorbents. *Renew Energy* 2009;34:1016–23. <https://doi.org/10.1016/j.renene.2008.08.003>.
- [33] Colombo P, Arcaro A, Francesconi A, Pavarin D, Rondini D, Debei S. Effect of hypervelocity impact on microcellular ceramic foams from a preceramic polymer. *Adv Eng Mater* 2003;5:802–5. <https://doi.org/10.1002/adem.200300397>.
- [34] Müller D, Knoll C, Gravogl G, Jordan C, Eitenberger E, Friedbacher G, et al. Medium-temperature thermochemical energy storage with transition metal ammoniates – a systematic material comparison. *Appl Energy* 2021;285:116470. <https://doi.org/10.1016/j.apenergy.2021.116470>.
- [35] Liu CY, Aika KI. Ammonia adsorption on alkaline earth halides as ammonia separation and storage procedure. *Bull Chem Soc Jpn* 2004;77:123–31. <https://doi.org/10.1246/bcsj.77.123>.
- [36] Yan T, Zhang H, Yu N, Li D, Pan QW. Performance of thermochemical adsorption heat storage system based on MnCl₂-NH₃ working pair. *Energy* 2022;239:122327. <https://doi.org/10.1016/j.energy.2021.122327>.
- [37] Li C, Wang X, Yang A, Chen P, Zhao T, Liu F. Polyethyleneimine-modified amorphous silica for the selective adsorption of CO₂/N₂ at high temperatures. *ACS Omega* 2021;6:35389–97. <https://doi.org/10.1021/acsomega.1c04743>.
- [38] Ali I, Burakova I, Galunin E, Burakov A, Mkrtychyan E, Melezhik A, et al. High-speed and high-capacity removal of methyl orange and malachite green in water using newly developed mesoporous carbon: kinetic and isotherm studies. *ACS Omega* 2019;4:19293–306. <https://doi.org/10.1021/ACSOMEGA.9B02669>.
- [39] Hao Y, Wang H, Han R, Liu C, Liu Q. Low concentration adsorption of ammonia using metal halide loaded biogas residue-based carbon materials. *Sep Purif Technol* 2025;352:128164. <https://doi.org/10.1016/j.seppur.2024.128164>.
- [40] Shen C, Shen L. Cyclic NH₃ adsorption-desorption characteristics of Cu-based metal halides as ammonia separation and storage procedure. *J Energy Inst* 2023;109. <https://doi.org/10.1016/j.joei.2023.101250>.
- [41] Cheung O, Bacsik Z, Liu Q, Mace A, Hedin N. Adsorption kinetics for CO₂ on highly selective zeolites NaKA and nano-NaKA. *Appl Energy* 2013;112:1326–36. <https://doi.org/10.1016/j.apenergy.2013.01.017>.
- [42] Ojuva A, Akhtar F, Tomsia AP, Bergström L. Laminated adsorbents with very rapid CO₂ uptake by freeze-casting of zeolites. *ACS Appl Mater Interfaces* 2013;5:2669–76. <https://doi.org/10.1021/am400122r>.
- [43] Kamran U, Shezad N, Park SJ, Rhee KY, You S, Akhtar F. Solvent-free valorization of sugarcane bagasse fibers into nitrogen-doped microporous carbons: efficient contenders for selective carbon dioxide capture. *J CO₂ Util* 2025;92. <https://doi.org/10.1016/j.jcou.2025.103033>.